Supplementary Material for

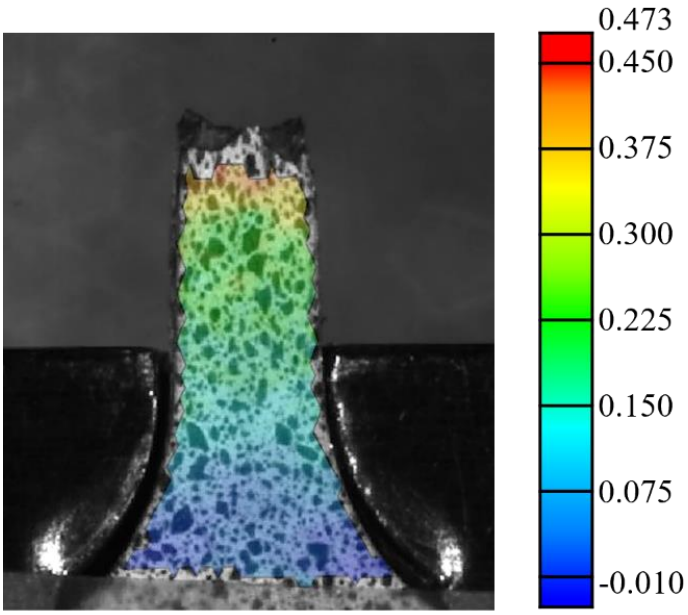

Fig. S1. Distribution of local true strain in the A900 sample after fracture, as captured by the DIC technique.

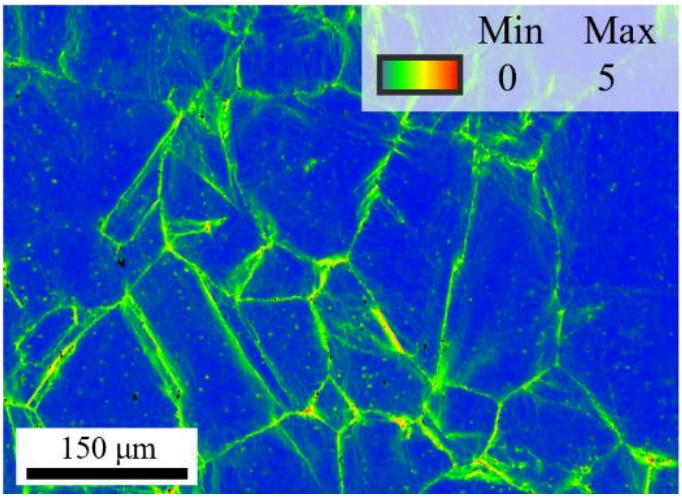

Fig. S2. KAM map of the HR sample.

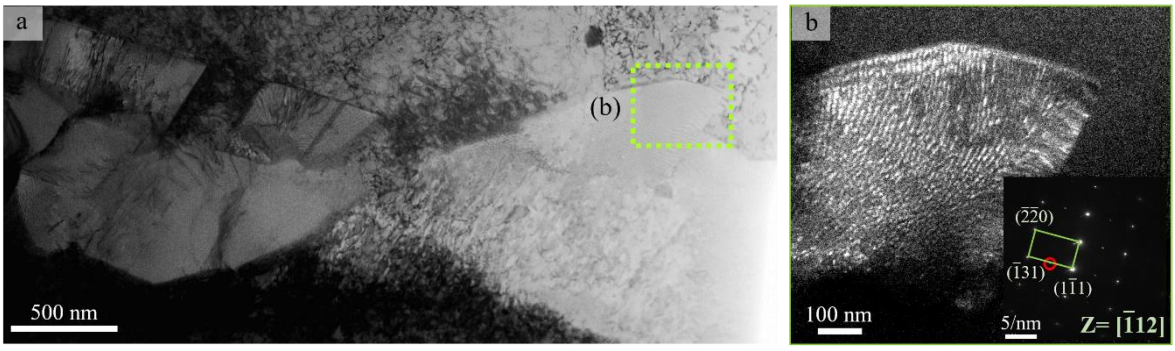

Fig. S3. (a) STEM image of the HR sample; (b) dark-field image of the local area in (a) with its SAED pattern. Dark-field images were obtained from the red-circled spot in the SEAD pattern.

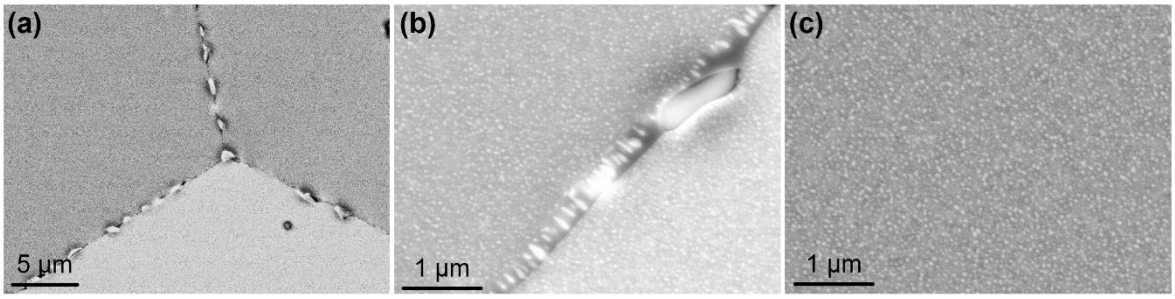

Fig. S4. SEM image of the as-cast sample at various magnifications: (a) 200×, (b) 5000×, and (c) 50,000×.

Table S1 Chemical compositions of precipitates in the A900 sample (at%).

		Ni	Co	Fe	Cr	Ti	Al
B2	Average	36.7	15.3	7.53	5.19	23.3	11.9
	Std. deviation	1.11	0.81	2.27	2.62	3.41	1.42
Continuous $L1_2$	Average	42.6	15.1	12.2	10.5	11.8	7.83
	Std. deviation	3.1	1.14	1.76	2.35	0.94	1.22
Discontinuous $L1_2$	Average	41.1	16.7	15.1	13.5	6.73	6.9
	Std. deviation	4.61	0.98	2.22	2.65	0.96	1.2

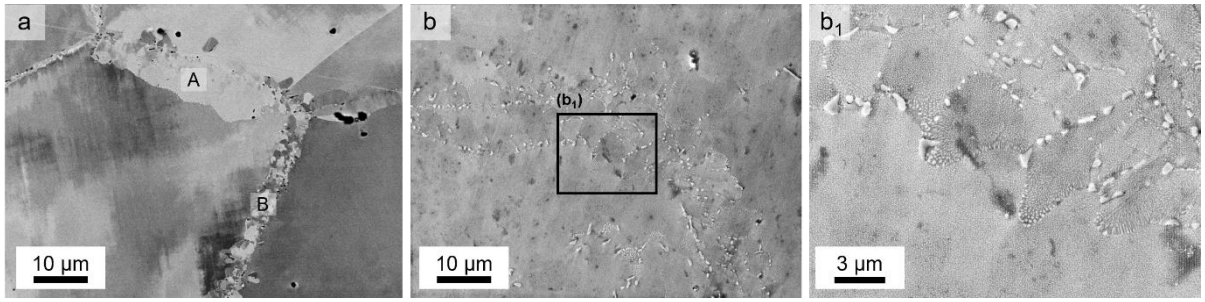

Fig. S5. SEM images of (a) the 10–minute heat treated sample (same position as Figure 9a); (b) the A900+AG sample (same position as Fig. 9(c)), and (c) a magnified image of (b) showing a convex shaped recrystallized grain with cellular $L1_2$ precipitates.

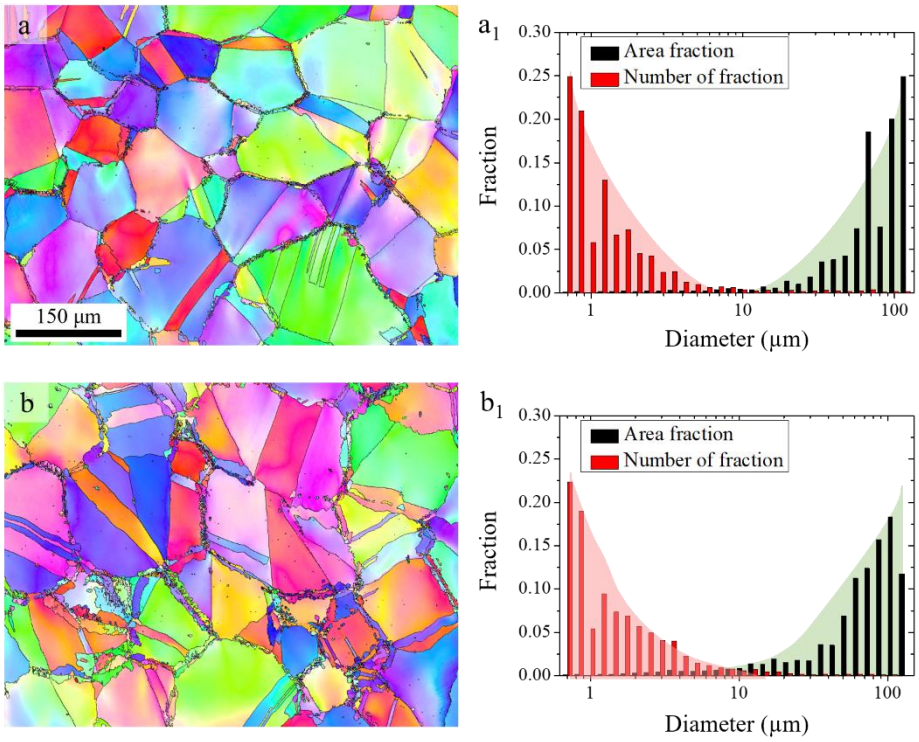

Fig. S6. EBSD images: IFP map and grain size distributions of samples annealed at 900 ℃ for (a) 10 min and (b) 3 h.

Precipitation Strengthening Mechanisms

Precipitation strengthening is classified into two mechanisms: (1) the Orowan bypass mechanism and (2) the dislocation shearing mechanism.

The Orowan bypass mechanism refers to the interaction between dislocations and precipitates, where dislocations bow around large precipitates, impeding their motion and contributing to overall strengthening [1]. This mechanism can be quantified by the following Eq. (1) and Eq. (2) [2]:

$$\Delta\sigma_{\mathrm{Oro}} = M \cdot \frac{0.4Gb}{\pi\lambda} \frac{\ln\frac{2\bar{r}}{b}}{\sqrt{1-\nu}}, \tag{1}$$

$$\lambda = \sqrt{\frac{4}{3}}\bar{r}\sqrt{\frac{\pi}{4f}-1}, \tag{2}$$

where M represents the Taylor factor for the FCC matrix (~ 3.06), G represents the shear modulus, b is the Burgers vector, ν is the Poisson's ratio (0.3), λ represents the inter-precipitate spacing, $\bar{r}$ represents the mean precipitate radius, and f is the volume fraction of the precipitate.

The dislocation shearing mechanism occurs when precipitates are nanoscale, typically below 20 nm in radius, and remain coherent with the matrix. Three factors contribute to this mechanism: coherent strengthening ($\Delta\sigma_{\mathrm{cs}}$), modulus strengthening ($\Delta\sigma_{\mathrm{ms}}$), and order strengthening ($\Delta\sigma_{\mathrm{os}}$). Coherency strengthening arises from the interaction between the strain-field of the coherent precipitate and the matrix [3]. Modulus strengthening is caused by the mismatch between the shear moduli of the precipitate and the matrix, leading to additional resistance to dislocation motion [3]. Ordering strengthening emerges due to the formation of an anti-phase boundary (APB) when dislocations shear through the precipitate. During the shearing process, the relative contributions of these mechanisms vary. Coherency and modulus strengthening dominate before the shearing, whereas order strengthening becomes predominant during the shearing process [4, 5]. The total contribution of the shearing strengthening mechanism is determined by comparing the sum of coherency and modulus strengthening with the order strengthening value. Among these, the overall strengthening contribution is governed by the largest value, as it defines the dominant strengthening mechanism at a given stage.

The strengthening contributions can be quantified using the following Eqs.(3–5) [3]

$$\Delta\sigma_{cs} = M{\cdot}\alpha_{\varepsilon}(G{\cdot}\varepsilon)^{3/2}\left(\frac{rf}{0.5Gb}\right)^{1/2}, \quad (3)$$

$$\Delta\sigma_{ms} = M{\cdot}0.0055(\Delta G)^{3/2}\left(\frac{2f}{G}\right)^{1/2}\left(\frac{r}{b}\right)^{(3m/2)-1}, \quad (4)$$

$$\Delta\sigma_{os} = M{\cdot}0.81\left(\frac{\gamma_{APB}}{2b}\right)\left(\frac{3\pi f}{8}\right)^{1/2}, \quad (5)$$

where M is the Talyor factor (3.06 for FCC materials), α_{ε} = 2.6 for FCC materials, G = 81 GPa is the shear modulus [6], ε is the constrained lattice parameter misfit (≈ 2/3·(Δa/a)), where Δa denotes the difference in lattice parameter between the $L1_2$ and FCC matrix, with Δa/a derived from reference [7]. r is the average precipitate diameter, f is the volume fraction of the $L1_2$ precipitate, b is the Burgers vector, ΔG is the modulus difference between the FCC matrix and $L1_2$ precipitates (81 − 77 = 4 GPa) [6], m is a constant value (= 0.85), and γ_{APB} is the antiphase boundary free energy of the precipitates.

Among these mechanisms, the largest contribution determines the overall precipitation strengthening effect through the shearing mechanism. To comprehensively evaluate all potential strengthening mechanisms, the contributions of precipitation strengthening were calculated for both the A900 and A900+AG samples, and the results were plotted as a function of precipitate radius in Fig. S7. The calculations based on the Orowan bypass mechanism indicate that precipitates with radii below 30 nm could theoretically contribute to a strengthening effect exceeding 1,000 MPa. However, this value does not align with the experimental results.

Comparative analysis of the coherency, modulus, and order strengthening components revealed that both specimens exhibit a critical radius of approximately 16 nm. For precipitates smaller than this critical radius, the strengthening contribution is dominated by the order-strengthening mechanism. Thus, the shearing mechanism—particularly order strengthening—is the most suitable model for quantifying the precipitation strengthening effect in these

samples.

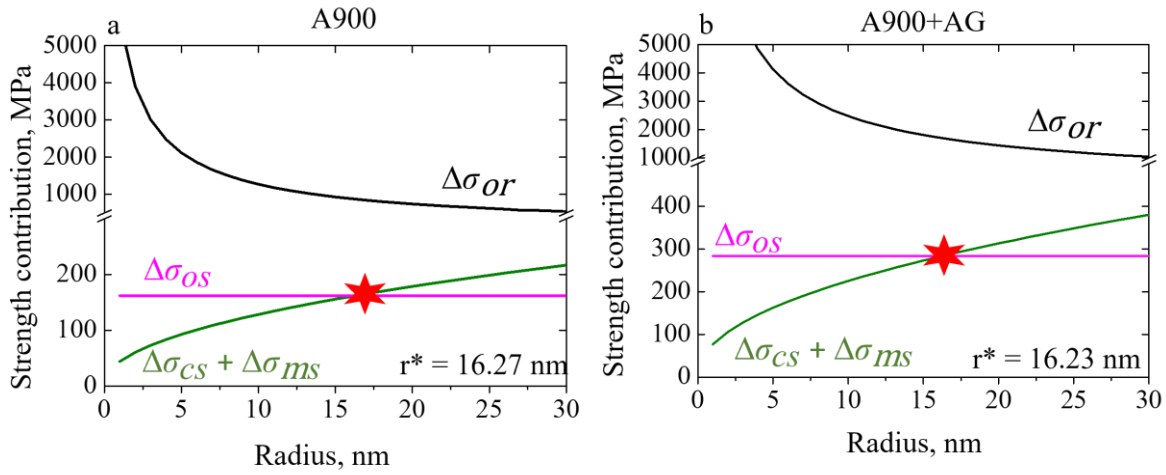

Fig. S7. Precipitate strengthening as a function of precipitate radius: (a) A900 sample and (b) A900+AG sample.

Nanoindentation and Microhardness Results of the Core–Shell Structure

Both nanoindentation and microhardness testing were conducted to evaluate the hardness difference between the core and shell regions. While nanoindentation offers high spatial resolution, we found that it is not sufficient for capturing the deformation resistance of the matrix, particularly when influenced by micron or submicron-scale deformation-related defects such as individual dislocations, dislocation cells, and pile-ups. Regardless of the indentation location, nanoindentation measurements remained relatively constant, displaying a random distribution without a clear trend, thereby complicating the assessment of strain partitioning effects. The insensitivity of nanoindentation measurements (Fig. S8) is likely due to the localized and highly flexible nature of deformation-related defects, which do not significantly alter the nanoscale elastic modulus. Because nanoindentation primarily captures nanoscale structural variations at the indentation site, it is highly sensitive to localized microstructural features and may not effectively capture broader mechanical property differences in heterogeneous materials. Furthermore, since slip transmission and dislocation pile-up at grain boundaries can either strengthen or weaken the material depending on boundary characteristics [8], nanoindentation may yield inconsistent or misleading hardness value.

Nanoindentation experiments were conducted at a peak load of 5 mN and a loading rate of 0.05 mN/s using a Nanoindenter (iMicro, KLA) with a Vickers indenter. According to the Hall-Petch relationship, decreasing grain size enhances a material's yield strength by increasing the resistance of grain boundaries to dislocation motion. While nanoindentation studies typically observe this effect in ultrafine-grained materials, the indentation depth must be comparable to or smaller than the grain size—typically below a few hundred nanometers—for this trend to be reliably measured [8, 9]. When grain sizes exceed several micrometers, nanoindentation becomes less effective in detecting grain boundary strengthening effects, as individual indentations are unlikely to interact with multiple grain boundaries [8]. Consequently, for micrometer-scale grains, nanoindentation measurements primarily reflect

local plasticity at the individual grain level rather than the overall Hall-Petch effect, leading to inconsistent hardness variations.

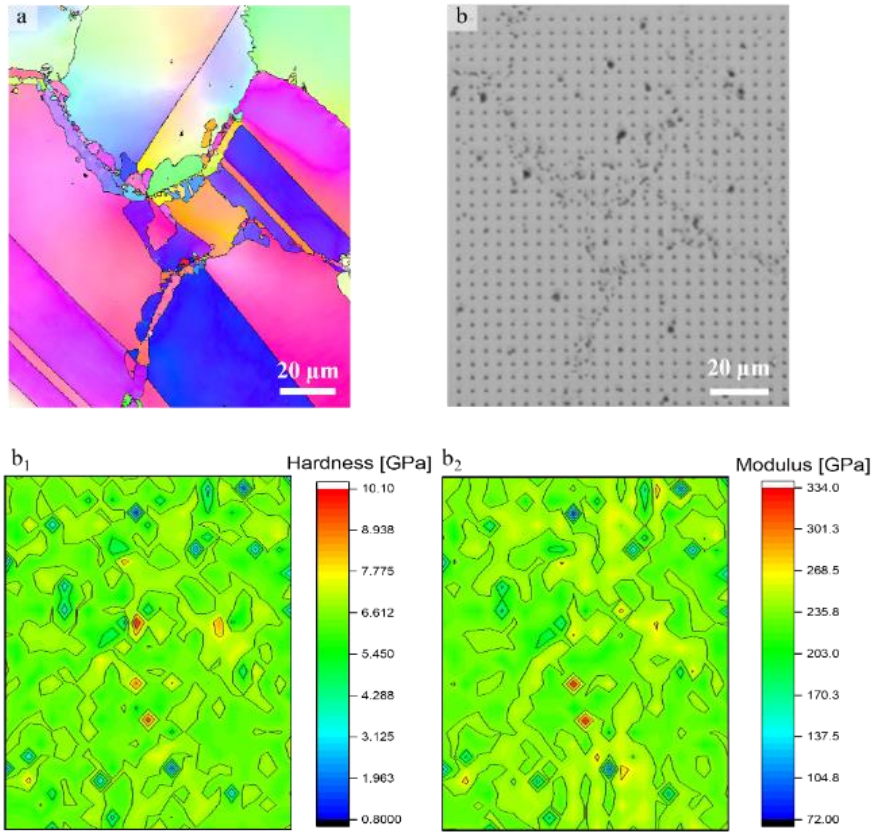

Fig. S8. Nanoindentation result for the A900 sample: (a) EBSD image before testing, (b) SEM image after testing, (b_1) hardness map, and (b_2) elastic modulus map.

In contrast, microhardness testing provided a clear and reliable distinction between the core and shell regions. The microhardness results (Fig. S9) revealed that the shell exhibits an average hardness of 283 ± 15 HV, whereas the core has a lower average hardness of 247 ± 13 HV, confirming mechanical heterogeneity. Unlike nanoindentation, which provides highly localized hardness values, microhardness measurements encompass a larger contact area, minimizing the influence of local microstructural fluctuations and better representing the bulk mechanical response.

Previous studies have highlighted the advantages of microhardness testing in

characterizing heterogeneous structures [10, 11]. Microhardness is particularly sensitive to grain size, phase distribution, and recrystallization effects, making it more effective for characterizing materials with complex microstructures [10]. Similarly, in heterogeneous structures containing regions with distinct grain sizes of approximately 13 μm and 42 μm, microhardness testing successfully differentiated the hardness of each region, further confirming its effectiveness in capturing mechanical variations in coarse-grained alloys [11].

The results of this study align with these findings, as microhardness clearly distinguished the mechanical contrast between the core and shell, whereas nanoindentation exhibited substantial variability. Therefore, for microscale heterogeneous materials, particularly those with coarse grains and precipitate-rich boundaries, microhardness testing provides a more reliable and representative assessment of mechanical property variations.

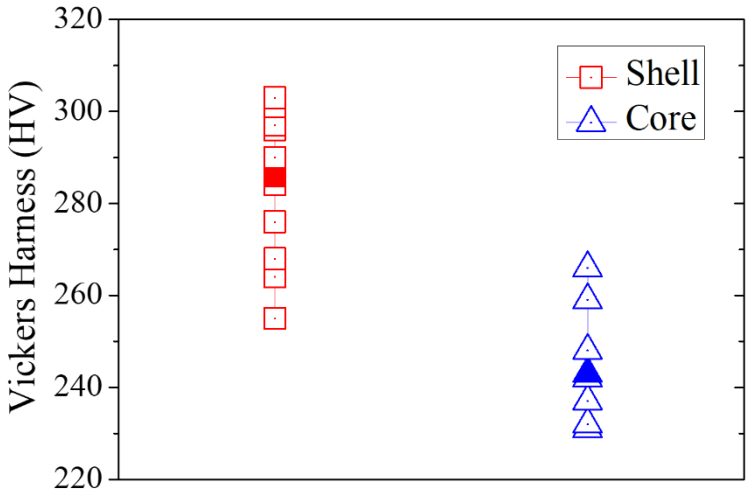

Fig. S9. Microhardness results of shell and core regions in the A900 sample (solid markers represent median values).

References

[1] H. Park, F. Haftlang, Y.U. Heo, J.B. Seol, Z. Wang, H.S. Kim, Nat. Commun. 15(1) (2024) 5757.

[2] F. Haftlang, P. Asghari-Rad, J. Moon, A. Zargaran, K.A. Lee, S.J. Hong, H.S. Kim, Scr. Mater. 202 (2021).

[3] E.A. Marquis, D.N. Seidman, D.C. Dunand, Acta Mater. 51(1) (2003) 285-287.

[4] D.N. Seidman, E.A. Marquis, D.C. Dunand, Acta Mater. 50(16) (2002) 4021-4035.

[5] J. Guo, B. Zhou, S. Qiu, H. Kong, M. Niu, J. Luan, T. Zhang, H. Wu, Z. Jiao, J. Mater. Sci. Technol. 166 (2023) 67-77.

[6] T. Pollock, A. Argon, Acta Metall. Mater. 40(1) (1992) 1-30.

[7] A. Kelly, R. Nicholson, Strengthening Methods in Crystals, Elsevier, 1971.

[8] B. Yang, H. Vehoff, Acta Mater. 55(3) (2007) 849-856.

[9] V. Paul, M. Wakeda, K. Ameyama, M. Ota-Kawabata, T. Ohmura, Materials 14(19) (2021) 5663.

[10] S. Baskutis, V. Vasauskas, A. Žunda, Mechanics 22(2) (2016) 85-89.

[11] R.E. Kim, E.S. Kim, G.M. Karthik, G.H. Gu, S.Y. Ahn, H. Park, J. Moon, H.S. Kim, Scr. Mater. 215 (2022) 114732.